

Contribution of anthropogenic and natural sources to atmospheric methane variability

P. Bousquet^{1,2}, P. Ciais¹, J. B. Miller^{3,4}, E. J. Dlugokencky³, D. A. Hauglustaine¹, C. Prigent⁵, G. R. Van der Werf⁶, P. Peylin⁷, E.-G. Brunke⁸, C. Carouge¹, R. L. Langenfelds⁹, J. Lathière¹, F. Papa^{5,10}, M. Ramonet¹, M. Schmidt¹, L. P. Steele⁹, S. C. Tyler¹¹ & J. White¹²

Methane is an important greenhouse gas, and its atmospheric concentration has nearly tripled since pre-industrial times¹. The growth rate of atmospheric methane is determined by the balance between surface emissions and photochemical destruction by the hydroxyl radical, the major atmospheric oxidant. Remarkably, this growth rate has decreased² markedly since the early 1990s, and the level of methane has remained relatively constant since 1999, leading to a downward revision of its projected influence on global temperatures. Large fluctuations in the growth rate of atmospheric methane are also observed from one year to the next², but their causes remain uncertain^{2–13}. Here we quantify the processes that controlled variations in methane emissions between 1984 and 2003 using an inversion model of atmospheric transport and chemistry. Our results indicate that wetland emissions dominated the inter-annual variability of methane sources, whereas fire emissions played a smaller role, except during the 1997–1998 El Niño event. These top-down estimates of changes in wetland and fire emissions are in good agreement with independent estimates based on remote sensing information and biogeochemical models. On longer timescales, our results show that the decrease in atmospheric methane growth during the 1990s was caused by a decline in anthropogenic emissions. Since 1999, however, they indicate that anthropogenic emissions of methane have risen again. The effect of this increase on the growth rate of atmospheric methane has been masked by a coincident decrease in wetland emissions, but atmospheric methane levels may increase in the near future if wetland emissions return to their mean 1990s levels.

The global growth rate of atmospheric methane (CH₄) decreased from nearly $+12 \pm 2$ p.p.b. yr⁻¹ in the 1980s to $+4 \pm 4$ p.p.b. yr⁻¹ in the last decade (all values are means \pm s.d.), but with large year-to-year variations² (Fig. 1a). A peak in growth rate occurred in 1991 in the tropics, followed by a large and abrupt drop in 1992, which began in the northern regions. The past few years have been marked by two positive growth-rate anomalies in 1997–1998 and in 2002–2003, which seem more pronounced north of 30°N than in the tropics.

To understand better why the growth rate of CH₄ has remained persistently smaller after the early 1990s, we have analysed the regional trends in CH₄ differences between sampling sites in the National Oceanic and Atmospheric Association (NOAA) global co-operative air sampling network² and the South Pole site, taken as a reference (Fig. 1b and Supplementary Information). This analysis

suggests that either northern CH₄ emissions have declined persistently since 1992 or that the destruction of CH₄ by the hydroxyl radical (OH) has increased north of 30°N. Several conflicting hypotheses have been proposed to explain interannual and long-term variations in atmospheric CH₄, focusing on wetland CH₄ emissions^{10,13,14}, anthropogenic CH₄ emissions⁵, wild fires^{6–9,15}, OH photochemistry^{3,4,11} and inter-annual wind changes¹². Various models have been used, but the contribution of each process has not been disentangled in a coherent framework, except for short periods^{6,16}. Our understanding of the current methane budget therefore remains plagued by very large uncertainties.

Atmospheric CH₄ measurements can be linked quantitatively to regional sources and sinks by inverse modelling. For the period 1984–2003, the CH₄ concentration responses to the action of OH sinks and regional surface sources were simulated each month with the three-dimensional chemistry transport model LMDZ-INCA¹⁷. The model was forced with interannual analysed winds¹⁸ and inter-annually varying OH concentrations¹⁹. Emissions of CH₄ from different regions of the globe and from distinct processes (see Methods), together with the photochemical sinks, were inferred, and their uncertainties reduced, by matching atmospheric observations within their uncertainties in a Bayesian formalism¹⁹. Clearly, uncertainties in the variations of OH concentrations limit our ability to infer accurately fluctuations in regional CH₄ emissions. The removal of CH₄ by OH nearly balances the sum of all surface sources, making the atmospheric CH₄ budget highly sensitive to OH changes. Thus, we constrained first the interannual variability of OH through a preliminary inversion of methyl chloroform atmospheric observations¹⁹. Contributions of monthly surface CH₄ sources and pre-optimized monthly OH sinks were then combined to fit optimally monthly averages of CH₄ measurements from a global network of 68 sampling sites. Long-term measurements of the ¹³C/¹²C ratio in CH₄ ($\delta^{13}\text{C-CH}_4$) were also used as an additional constraint for the partitioning of microbial-, biomass-burning- and fossil-fuel-related CH₄ sources. We performed a control inversion, supplemented by an ensemble of 17 sensitivity inversions (see Methods).

We found that the year-to-year CH₄ regional flux changes (or anomalies) can be more robustly inverted than their mean values, a result similar to CO₂ inversions^{20,21}. Indeed, among the different sensitivity inversions, the spread of regional flux anomalies is more than a factor of two smaller than the spread of long-term mean fluxes. In other words, possible biases in the inversions seem to have low interannual variability. To illustrate this point, we tested the impact

¹Laboratoire des Sciences du Climat et de l'Environnement, IPSL-LSCE, CEA-CNRS-UVSQ, F-91191, France. ²Université de Versailles Saint Quentin en Yvelines, F-78035, France.

³NOAA Earth System Research Laboratory, Global Monitoring Division, Boulder, Colorado 80305-3328, USA. ⁴Cooperative Institute for Research in Environmental Science, Campus Box 216, University of Colorado, Boulder, Colorado 80309, USA. ⁵LERMA, Observatoire de Paris, F-75014, France. ⁶Faculty of Earth and Life Sciences, Vrije Universiteit, Amsterdam, The Netherlands. ⁷Laboratoire de Biogéochimie Isotopique, LBI, F-78026, France. ⁸South African Weather Service, Stellenbosch 7599, South Africa. ⁹CSIRO, Marine and Atmospheric Research, Victoria 3195, Australia. ¹⁰NASA-GISS-Columbia University, New York, New York 10025, USA. ¹¹Earth System Science Department, University of California, Irvine, California 92697, USA. ¹²Institute of Arctic and Alpine Research, University of Colorado, Boulder, Colorado 80309, USA.

of adding an additional methane source from plants²² with an *a priori* value of $+150 \pm 60 \times 10^{12}$ grams of CH_4 per year ($\text{Tg of CH}_4 \text{ yr}^{-1}$). The long-term-mean inverted fluxes were strongly affected by this 'intrusion' of this new source, but the atmospheric measurements remained fitted and the global budget was conserved, after a reduction in plant and other source emissions (-30%) within their uncertainties. The sparseness of the tropical network, along with large uncertainties on prior emissions, prevents us from verifying the existence of long-term CH_4 emissions by plants. Adding plants in the *a priori* CH_4 sources mix, however, did not alter the inferred anomalies in the 1990s (see Supplementary Information). Given their robustness, the flux anomalies are therefore the primary focus of the following analysis.

We found that fluctuations in wetland emissions are the dominant contribution to interannual variability in surface emissions ($\pm 12 \text{ Tg of CH}_4 \text{ yr}^{-1}$), explaining 70% of the global emission anomalies over the past two decades, as compared with only 15% contributed by biomass burning (Fig. 2). This result disagrees with previous studies suggesting a dominant role of fires^{6–9,14}. As an independent check on the inverted wetland variability, we applied a simple wetland flux model (see Supplementary Information) based on ref. 23 and driven by interannually varying climate data¹⁸ and by estimates of remotely sensed changes in flooded areas for the period 1993–2001. There is good agreement in the magnitude of the wetland flux anomalies between the bottom-up and inversion results (normalized standard

deviation (NSD) = 1.1; see Methods), as seen in Fig. 2. The correlation between the two estimates is improved when a 3-month lag is applied to the inversion results ($r^2 = 0.4$, $P = 0.06$). In 1993–2001, wetland emissions in the bottom-up model show a persistent negative trend of $2.5 \text{ Tg of CH}_4 \text{ yr}^{-1}$, in response to a marked decrease in flooded area worldwide (at a rate of $-1.1\% \text{ yr}^{-1}$ for a mean area of $4.2 \times 10^6 \text{ km}^2$), mostly in temperate and tropical Asia and in tropical South America²³. The inversion infers decreasing wetland emissions after 1993, but with a smaller trend ($-0.6 \text{ Tg of CH}_4 \text{ yr}^{-1}$). Shrinking wetland areas may reflect recurrent dryness observed in the tropics after 1990 (ref. 18), and northward after 1999 (ref. 24).

The inversion attributes global variations in the biomass-burning emissions of the order of $\pm 3.5 \text{ Tg of CH}_4 \text{ yr}^{-1}$ (Fig. 2). In 1989–2002, these anomalies are in very good agreement with independent estimates⁹ derived from remote sensing data after 1996 ($r^2 = 0.6$, $P = 0.012$; NSD = 0.8) and inferred from global CO variations before 1996 ($r^2 = 0.4$, $P = 0.08$; NSD = 1.2; see Supplementary Information). Such agreement is remarkable, given that the *a priori* biomass-burning fluxes prescribed to the inversion are constant from year to year. The members of the inversion ensemble that include $\delta^{13}\text{C}-\text{CH}_4$ observations agree best with the magnitude of the bottom-up anomalies⁹ (NSD = 1.1). At face value, these 'isotopic' inversions

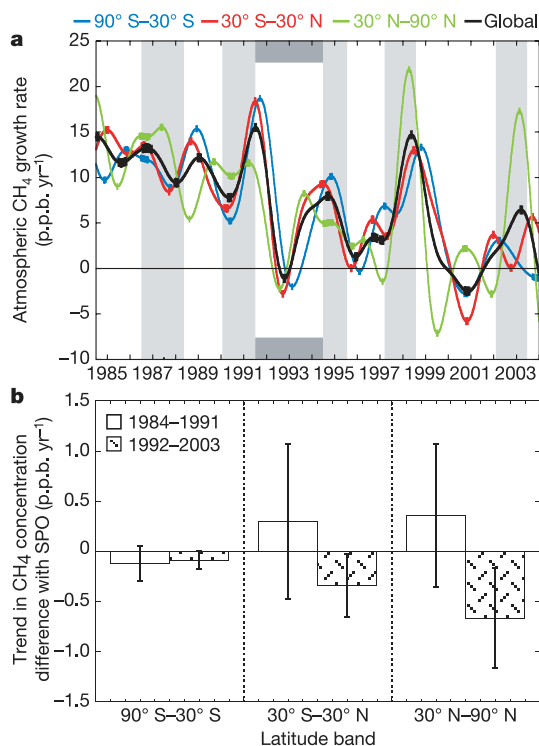


Figure 1 | Variability and trends in atmospheric CH_4 over the past two decades. **a**, Interannual variations in the growth rate of atmospheric CH_4 (p.p.b. yr^{-1}) in the period 1984–2003, calculated by using data from the NOAA air sampling sites used in the inversion model (maximum of 50 sites). Black, global growth rate; blue, Southern Hemisphere $<30^\circ\text{S}$; red, 30°S to 30°N (tropics); green, Northern Hemisphere $>30^\circ\text{N}$; light grey, El Niño episodes; dark grey, anomaly following the Pinatubo climate anomaly. **b**, Average trends in the CH_4 difference (in p.p.b. yr^{-1}) between sites grouped in three latitude bands and the South Pole site (SPO). Trends were calculated by using monthly deseasonalized observations. Open bars indicate trends in ΔCH_4 in the 1980s (1984–1991), when the global growth rate was $+12 \pm 2 \text{ p.p.b. yr}^{-1}$; hatched bars indicate trends in ΔCH_4 after 1993, when the global growth rate was $4 \pm 4 \text{ p.p.b. yr}^{-1}$. Error bars are 1 s.d. of the calculated trends in differences for the NOAA sites.

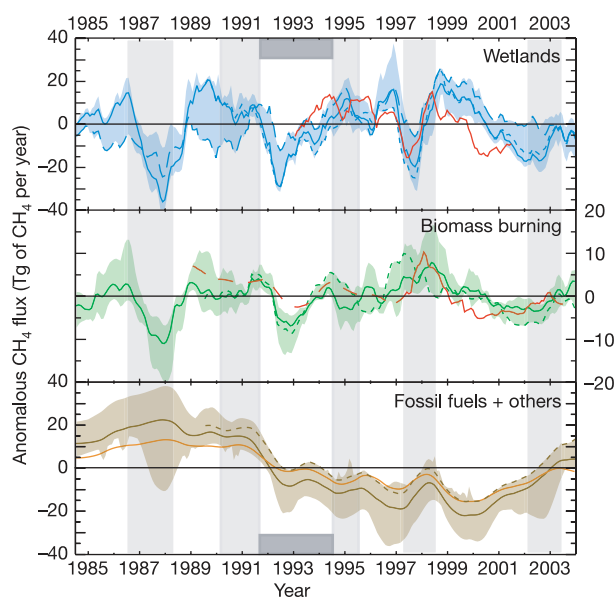


Figure 2 | Variations in CH_4 emissions attributed to different processes. Shown are the interannual global CH_4 flux anomalies (in $\text{Tg of CH}_4 \text{ yr}^{-1}$; note different y-axis scales) broken down into different processes. Unbroken lines of each sub-panel indicate the member of the ensemble with only CH_4 observations (control inversion, 68 sites); broken lines of each sub-panel indicate the member of the ensemble with both CH_4 observations (68 sites) and $\delta^{13}\text{C}-\text{CH}_4$ observations (13 sites after 1998; 4 sites after 1989). Blue indicates wetlands (including rice agriculture); dashed blue line represents wetland anomaly inferred in the extreme case where OH is maintained constant from year to year. Green indicates biomass burning. Brown indicates energy-related sources (fossil fuels, industry, bio-fuels) and other sources (landfills and waste, ruminants, termites, ocean, plants). Unbroken orange line represents the specific contribution of fossil-fuel emissions alone. Red lines indicate set of bottom-up estimates of CH_4 flux anomalies obtained from a wetland flux model driven by remotely sensed flooded area data²², and from a fire model driven by remote sensing measurements after 1997 (ref. 9), and extrapolated using atmospheric carbon monoxide trends before that date (see Supplementary Information). The anomalies are calculated by subtracting the long-term mean CH_4 flux over the whole period (1984–2003) from the deseasonalized (12-month running mean) monthly flux in each region. Shaded areas represent the spread of an ensemble of 18 inversions (each using *a priori* OH fields pre-optimized from methyl chloroform).

place a strong (tropical) release of CH_4 by fires in 1997, six months earlier than inferred from the remote sensing data (Fig. 2).

The regional patterns of surface CH_4 emissions indicate that most of the global year-to-year variability lies in the tropics (Fig. 3). By contrast, the northern regions show smoother variations, but with systematically less emissions in the 1990s than in the 1980s, except for 1997–1998 and 2002–2003, consistent with Fig. 1b. The variability in CH_4 removal by OH radicals¹⁹ is also dominated by the tropics, where photochemistry remains active all year (Fig. 3). We found that the years 1987–1988, 1991–1992, 1997–1998 and 2001–2002 correspond to abnormally weaker CH_4 destruction by OH in the tropics. In the inversion, a compensation effect exists between the magnitude of methyl-chloroform-derived changes in OH and inverted CH_4 surface emissions, because the sum of the two must equal the observed atmospheric accumulation. Thus, biases in OH changes

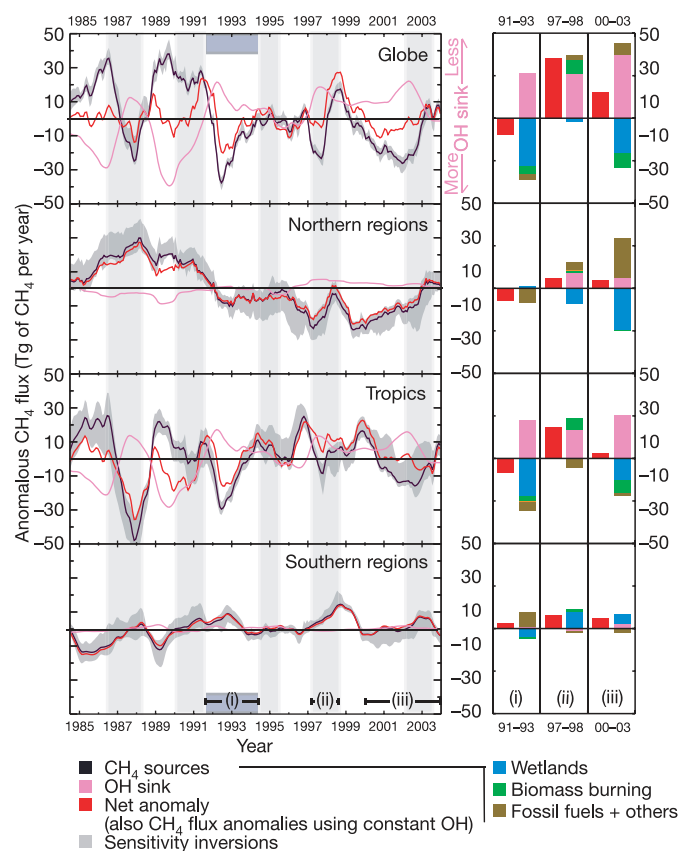


Figure 3 | Large-scale regional variations in CH_4 emissions and OH sink. Left, interannual flux anomalies (in $\text{Tg of CH}_4 \text{ yr}^{-1}$) broken down into three large regions²⁷ for the control inversion: northern regions, tropics and southern regions. Black indicates surface emission anomaly, with grey uncertainty estimates based on the spread of the ensemble of 18 inversions (each using *a priori* OH variations pre-optimized from methyl chloroform). Pink indicates anomalies in CH_4 removal by OH (negative values mean more CH_4 removal). Red indicates anomalies in the net CH_4 budget in each band; that is, the sum of surface emissions and OH removal. This red line also represents what the surface emissions anomalies would be in the extreme case where OH is maintained constant from year to year. Right, changes in surface emissions and in the OH removal term within each large region during selected remarkable episodes analysed in the text: the drop in CH_4 growth rate of 1991–1993; the high CH_4 growth rate of the 1997–1998 largest El Niño event; and the persistent low mean atmospheric growth rate of 2000–2003. The 1991–1993 anomaly is discussed after subtraction of the mean flux over 1984–2003. The 1997–1998 and the 2000–2003 anomalies are discussed after subtraction of the mean flux over 1993–2003. Quantities refer to the full episode (Tg of CH_4). Each source is coloured as in Fig. 2. A positive bar indicates an increase in surface emission and a decrease in OH removal.

could account for some of the variability that we attributed to wetlands. In the extreme case where OH interannual variability is set at zero, the fluctuations of tropical wetland emissions are dampened by 50%, especially in the 1980s, when methyl chloroform data suggest large OH variability¹⁹.

We analysed in detail two key perturbations of the CH_4 budget in the past two decades (Fig. 3). First, we studied the drop in growth rate in 1991–1993. This period is particularly intriguing because of the potentially confounding effects of three factors: (1) reduced photochemical production caused by changes in ultraviolet radiation associated with volcanic aerosols emitted in the eruption of the Mount Pinatubo in June 1991; (2) the widespread Northern Hemisphere cooling that followed²⁵; and (3) the economic collapse of the former Soviet Union. The first factor should decrease OH, causing CH_4 to increase. Indeed, we inferred a decrease in tropical OH by 5% from the methyl chloroform data¹⁹, as suggested by Fig. 1b and previous studies⁴. The two other factors should reduce wetland and fossil-fuel emissions respectively, causing atmospheric CH_4 to decrease. Overall, we attribute the 1991–1993 spike in growth rate, a -10 Tg of CH_4 event (Fig. 3), to a large decrease in emissions ($-36 \pm 6 \text{ Tg of CH}_4$) partly offset by a reduction in the OH sink intensity ($+26 \text{ Tg of CH}_4$). Sources that were reduced in that period are predominantly northern and tropical wetlands ($-24 \pm 6 \text{ Tg of CH}_4$) and anthropogenic sources ($-10 \pm 5 \text{ Tg of CH}_4$). Decreased biomass-burning emissions had a much smaller role ($-5 \pm 2 \text{ Tg of CH}_4$). This inversion result agrees well with an independent study showing reduced boreal wetland emissions due to cooler and dryer conditions¹⁰, and reduced northern anthropogenic emissions²⁶.

Second, we investigated the period 1997–1998, which corresponds to the largest El Niño on record. At that time, widespread dryness caused increases of fires in the tropical zone and in boreal regions of Eurasia⁹. In particular, large abnormal peat fires in Indonesia could have released huge amounts of CH_4 to the atmosphere from smouldering combustion¹⁵. A previous study⁹ estimated an anomalous fire source of $+11.5 \text{ Tg of CH}_4$ in 1997–1998 (Fig. 3), which agrees well with the inversion estimates ($+8 \pm 2 \text{ Tg of CH}_4$ in the tropics and $+2 \pm 1 \text{ Tg of CH}_4$ in northern regions). A larger decrease in OH concentration, possibly also caused by large emissions of carbon monoxide¹⁶ and other reactive carbon compounds by fires⁷, is found to contribute to a faster growth of CH_4 by an additional $+26 \text{ Tg of CH}_4$. Natural wetland emissions remained on average stable over the whole 1997–1998 period. However, there was a significant dip in 1997 for the northern regions wetlands ($-9 \pm 5 \text{ Tg of CH}_4$), followed by an increase in 1998 ($+10 \pm 5 \text{ Tg of CH}_4$) in the southern regions (Fig. 3). This shift in regional wetland emissions is fully consistent with the succession of regionally dryer and wetter climate conditions¹⁸.

Finally, we analysed why the global growth rate of atmospheric CH_4 remained low after the drop in 1991–1993 (ref. 4). After 1993, decreasing global emissions at a rate of $-1.0 \pm 0.2 \text{ Tg of CH}_4 \text{ yr}^{-1}$ are required to match a small average growth rate of $+4 \pm 4 \text{ p.p.b. yr}^{-1}$, in the presence of (slightly) decreasing OH (Fig. 3). The inversion attributes this signal to decreasing anthropogenic emissions, in particular to the northern fossil source (Fig. 3). This is in qualitative agreement with the latitudinal CH_4 differences analysed in Fig. 1b. After 1999, however, anthropogenic emissions increase again, especially in north Asia. This may reflect the booming Chinese economy. By 2003, we find that anthropogenic emissions recovered to their levels in the early 1990s. Without a coincident and important drop in northern wetland emissions after 1999 (Fig. 2) associated with dryer conditions²⁴, the growth rate of atmospheric CH_4 would therefore have increased much more rapidly. This suggests that the slow-down in CH_4 growth rate observed from the early 1990s may represent only a temporary pause in the human-induced secular increase in atmospheric CH_4 .

Better knowledge of the current CH_4 budget helps to reduce uncertainties in future projections of climate change and tropospheric

ozone evolution and to design effective mitigation strategies. Atmospheric long-term measurements and inverse models currently provide key information for assessing CH₄ emission trends at the global to subcontinental scale. Given uncertainties in surface emissions and OH distribution, however, using this approach at the regional or country scale remains challenging and requires an observational network that is dense in space and time²⁷. In the future, the combined use of improved emission inventories, isotopic observations and global space-borne measurements of column-integrated CH₄ should help better to quantify regional sources, to separate natural from anthropogenic processes, and to verify the effectiveness of CH₄ mitigation policies.

METHODS

Inversion model setup. The inverse methodology has been fully described¹⁹ through the example of OH field optimization against methyl chloroform observations. For CH₄, surface emissions are optimized each month for 11 land regions (those defined in ref. 28), one global ocean region, and up to ten processes over each land region (emissions from bogs, swamps, tundra, termites, fossil fuel and industry, gas, bio-fuel, ruminant animals, landfills and waste, and soil uptake). This spatial partition enables us to perform both geographically based and process-based analyses. On a geographical basis, the optimized emissions were further aggregated, after inversion, over three large regions: northern regions (boreal & temperate North America, boreal & temperate Asia, and Europe, roughly >30°N), tropical regions (tropical America, north and South Africa, tropical Asia), and southern regions (temperate South America and Oceania, roughly <30°S). We used the optimized interannual four-dimensional distribution of OH from ref. 19. The variations in OH are pre-optimized from methyl chloroform data using interannual winds and chemistry (see Supplementary Information). In this procedure, the inferred interannual OH fields also depend on methyl chloroform sources. Uptake of CH₄ by soils is optimized as an independent sink, but we do not explicitly solve for the stratospheric sink of CH₄ but assume that it is included in the removal by the stratospheric OH radicals of the INCA model¹⁷.

Atmospheric CH₄ observations, from roughly weekly air samples collected in flasks, were inverted as monthly means. Uncertainties in the monthly means were taken from the GLOBALVIEW-CH₄ data product²⁹, when available, or from submonthly variability in the measurements. In total, data from 68 sites from different networks were collected and used; 75% was contributed by the NOAA network. Offsets between different observing networks were accounted for by using intercomparison round-robin information reported in GLOBALVIEW-CH₄. The sampling periods for each site, and data uncertainties, are given in Supplementary Table A2. Atmospheric δ¹³C-CH₄ flask data from 13 NOAA sites were used in the inversion for the 1998–2004 period (Supplementary Table A2). The δ¹³C-CH₄ values were measured by INSTAAR at the University of Colorado³⁰. At four sites (Point Barrow, Mauna Loa, Samoa and South Pole), the NOAA observations were merged with those from the SIL network³¹ to extend the time series for the period 1989–2004. The gap in δ¹³C-CH₄ data in the period with no observations in 1996–1997 was filled by interpolation, and the interpolated values associated with a large *a priori* uncertainty in the inversion. At Niwot Ridge, the UCI network time-series³² was used to extend the atmospheric δ¹³C-CH₄ record back to 1994. Although isotopic ratios are monitored at only 13 sites, they are expected to constrain usefully the partitioning of CH₄ sources according to their mean isotopic signature: biomass burning (about –20‰ for C-3 plants; about –12‰ for C-4 plants), all bacterial processes (about –60‰) and fossil-fuel-related sources (about –40‰), the atmosphere being close to –47‰ on average. The carbon isotopes measurements are relative to Vienna Pee Dee Belemnite (VPDB).

The inversion of CH₄ fluxes accounts for the fact that CH₄ removal by OH radicals is a nonlinear function of surface CH₄ emissions, by iteratively applying the forward and the inverse transport chemistry model up until convergence is reached for the OH removal of CH₄. In inversions using δ¹³C-CH₄ data, we account for the fact that transport and chemistry of δ¹³C-CH₄ is nonlinear by solving iteratively for both the underlying CH₄ source magnitude and its isotopic composition, as in ref. 33.

Sensitivity tests. The settings of the inversion model that were varied in the sensitivity tests were (1) the *a priori* error on regional fluxes; (2) the *a priori* error on the atmospheric CH₄ and δ¹³C-CH₄ measurements; (3) the number of land regions to be optimized; (4) the size of the atmospheric network; (5) the use of non interannual transport; (6) the uses of non-interannual OH; (7) the introduction of an additional source due to possible CH₄ emission by plants²². See Supplementary Table A2 for a complete description of the 18 inversions performed.

NSD. The normalized standard deviation (NSD) is calculated as the ratio between the s.d. of the monthly deseasonalized inverted CH₄ flux anomaly and the s.d. of the same anomaly calculated by the bottom-up model. An NSD value of 1 indicates a similar variability between the inversion and the bottom-up model.

Received 10 April; accepted 3 August 2006.

1. IPCC. *Climate Change 2001: The Scientific Basis. Contribution of Working Group I to the Third Assessment Report of the Intergovernmental Panel on Climate Change* (eds Houghton, J. T. et al.) (Cambridge Univ. Press, Cambridge and New York, 2001).
2. Dlugokencky, E. J. et al. Atmospheric methane levels off: temporary pause or a new steady-state? *Geophys. Res. Lett.* **30**, 1992, doi:10.1029/2003GL018126 (2003).
3. Dentener, F. et al. Interannual variability and trend of CH₄ lifetime as a measure for OH changes in the 1979–1993 time period. *J. Geophys. Res.* **108**, 4442, doi:10.1029/2002JD002916 (2003).
4. Dlugokencky, E. J. et al. Changes in CH₄ and CO growth rates after the eruption of Mt Pinatubo and their link with changes in tropical tropospheric UV flux. *Geophys. Res. Lett.* **23**, 2761–2764 (1996).
5. Dlugokencky, E. J. et al. A dramatic decrease in the growth-rate of atmospheric methane in the Northern-Hemisphere during 1992. *Geophys. Res. Lett.* **21**, 507–507 (1994).
6. Langenfelds, R. L. et al. Interannual growth rate variations of atmospheric CO₂ and its δ C-13, H-2, CH₄, and CO between 1992 and 1999 linked to biomass burning. *Glob. Biogeochem. Cycles* **16**, 1048, doi:10.1029/2001GB001466 (2002).
7. Manning, M. R., Lowe, D. C., Moss, R. C., Bodeker, G. E. & Allan, W. Short-term variations in the oxidizing power of the atmosphere. *Nature* **436**, 1001–1004 (2005).
8. Page, S. E. et al. The amount of carbon released from peat and forest fires in Indonesia during 1997. *Nature* **420**, 61–65 (2002).
9. Van der Werf, G. R. et al. Continental-scale partitioning of fire emissions during the 1997 to 2001 El Niño/La Niña period. *Science* **303**, 73–76 (2004).
10. Walter, B. P., Heimann, M. & Matthews, E. Modeling modern methane emissions from natural wetlands 2. Interannual variations 1982–1993. *J. Geophys. Res.* **106**, 34207–34219 (2001).
11. Wang, J. S. et al. A 3-D model analysis of the slowdown and interannual variability in the methane growth rate from 1988 to 1997. *Glob. Biogeochem. Cycles* **18**, 3011, doi:10.1029/2003GB002180 (2004).
12. Warwick, N. J., Bekki, S., Law, K. S., Nisbet, E. G. & Pyle, J. A. The impact of meteorology on the interannual growth rate of atmospheric methane. *Geophys. Res. Lett.* **29**, 1947, doi:10.1029/2002GL015282 (2002).
13. Chen, Y. H. & Prinn, R. G. Estimation of atmospheric methane emissions between 1996 and 2001 using a three-dimensional global chemical transport model. *J. Geophys. Res.* **111**, doi:10.1029/2005JD006058 (2006).
14. Mikaloff Fletcher, S. E. M., Tans, P. P., Bruhwiler, L. M., Miller, J. B. & Heimann, M. CH₄ sources estimated from atmospheric observations of CH₄ and its C-13/C-12 isotopic ratios: 1. Inverse modeling of source processes. *Glob. Biogeochem. Cycles* **18**, GB4004, doi:10.1029/2004GB002223 (2004).
15. Simmonds, P. G. et al. A burning question. Can recent growth rate anomalies in the greenhouse gases be attributed to large-scale biomass burning events? *Atmos. Environ.* **39**, 2513–2517 (2005).
16. Butler, T. M., Rayner, P. J., Simmonds, I. & Lawrence, M. G. Simultaneous mass balance inverse modeling of methane and carbon monoxide. *J. Geophys. Res.* **110**, D21310, doi:10.1029/2005JD006071 (2005).
17. Hauglustaine, D. A. et al. Interactive chemistry in the Laboratoire de Meteorologie Dynamique general circulation model: description and background tropospheric chemistry evaluation. *J. Geophys. Res.* **109**, D04314, doi:10.1029/2003JD003957 (2004).
18. Uppala, S. M. et al. The ERA-40 reanalysis. *Q. J. R. Meteorol. Soc.* **131**, 2961–3012 (2005).
19. Bousquet, P., Hauglustaine, D. A., Peylin, P., Carouge, C. & Ciais, P. Two decades of OH variability as inferred by an inversion of atmospheric transport and chemistry of methyl chloroform. *Atmos. Chem. Phys.* **5**, 2635–2656 (2005).
20. Bousquet, P. et al. Regional changes in carbon dioxide fluxes of land and oceans since 1980. *Science* **290**, 1342–1346 (2000).
21. Rodenbeck, C., Houweling, S., Gloor, M. & Heimann, M. CO₂ flux history 1982–2001 inferred from atmospheric data using a global inversion of atmospheric transport. *Atmos. Chem. Phys.* **3**, 1919–1964 (2003).
22. Keppler, F., Hamilton, J. T. G., Braß, M. & Rockmann, T. Methane emissions from terrestrial plants under aerobic conditions. *Nature* **439**, 187–191 (2006).
23. Prigent, C., Matthews, E., Aires, F. & Rossow, W. B. Remote sensing of global wetland dynamics with multiple satellite data sets. *Geophys. Res. Lett.* **28**, 4631–4634, doi:10.1029/2001GL013263 (2001).
24. Hoerling, M. & Kumar, A. The perfect ocean for drought. *Science* **299**, 691–694 (2003).
25. Hansen, J., Ruedy, R., Sato, M. & Reynolds, R. Global surface air temperature in 1995: return to pre-Pinatubo level. *Geophys. Res. Lett.* **23**, 1665–1668 (1996).
26. Dlugokencky, E. J., Steele, L. P., Lang, P. M. & Masarie, K. A. The growth-rate and distribution of atmospheric methane. *J. Geophys. Res.* **99**, 17021–17043 (1994).

27. Bergamaschi, P. *et al.* Inverse modelling of national and European CH₄ emissions using the atmospheric zoom model TM5. *Atmos. Chem. Phys.* **5**, 2431–2460 (2005).
28. Gurney, K. R. *et al.* Towards robust regional estimates of CO₂ sources and sinks using atmospheric transport models. *Nature* **415**, 626–630 (2002).
29. GLOBALVIEW-CH₄. *Cooperative Atmospheric Data Integration Project—Methane* CD-ROM (NOAA/CMDL, Boulder, CO, 2005).
30. Miller, J. B. *et al.* Development of analytical methods and measurements of C-13/C-12 in atmospheric CH₄ from the NOAA Climate Monitoring and Diagnostics Laboratory global air sampling network. *J. Geophys. Res.* **107**, 4178, doi:10.1029/2001JD000630 (2002).
31. Quay, P. *et al.* The isotopic composition of atmospheric methane. *Glob. Biogeochem. Cycles* **13**, 445–461 (1999).
32. Tyler, S. C. *et al.* Stable carbon isotopic composition of atmospheric methane: a comparison of surface level and free tropospheric air. *J. Geophys. Res.* **104**, 13895–13910 (1999).
33. Hein, R., Crutzen, P. J. & Heimann, M. An inverse modeling approach to investigate the global atmospheric methane cycle. *Glob. Biogeochem. Cycles* **11**, 43–76 (1997).

Supplementary Information is linked to the online version of the paper at www.nature.com/nature.

Acknowledgements We thank P. Rayner, F. Chevallier and F.-M. Breon for comments on the manuscript, and P. Quay for published $\delta^{13}\text{C}$ -CH₄

measurements for the period 1989–1995. Atmospheric CH₄ measurements from Réseau Atmosphérique de Mesure des Composés à Effet de Serre (RAMCES) at Laboratoire des Sciences du Climat et de l'Environnement (LSCE) were partly funded by Institut National des Sciences de l'Univers (INSU). All calculations were realized with Commissariat à l'Energie Atomique (CEA), Centre National de la Recherche Scientifique (CNRS), Institut Pierre Simon Laplace (IPSL) and LSCE computers and support. The development of the Global Fire Emissions Dataset (GFED) used here was supported by a grant from the National Aeronautics and Space Administration (NASA).

Author Contributions The main contributions of each author are: P.B.: inversions, data analysis and coordination. P.C.: inverse method and manuscript improvements. J.B.M.: CH₄ and $\delta^{13}\text{C}$ -CH₄ data analysis and inversion analysis. E.J.D.: CH₄ measurements and manuscript improvements. D.A.H.: chemistry-transport model and manuscript improvements. C.P. and F.P.: satellite retrievals of flooded areas. G.R.V.d.W.: CH₄ emissions from fires. P.P. and C.C.: inversion method. R.L.L.: CH₄ measurements and manuscript improvements. E.G.B., M.R., M.S., L.P.S. and S.C.T.: CH₄ measurements. J.L.: plant source analysis. J.W.: $\delta^{13}\text{C}$ -CH₄ measurements.

Author Information Reprints and permissions information is available at www.nature.com/reprints. The authors declare no competing financial interests. Correspondence and requests for materials should be addressed to P.B. (philippe.bousquet@cea.fr).

Preserving the evolutionary potential of floras in biodiversity hotspots

Félix Forest^{1,2,3*}, Richard Grenyer^{3*}, Mathieu Rouget⁴, T. Jonathan Davies^{5,6}, Richard M. Cowling⁷, Daniel P. Faith⁸, Andrew Balmford⁹, John C. Manning¹, Şerban Procheş¹⁰, Michelle van der Bank¹¹, Gail Reeves¹, Terry A. J. Hedderson² & Vincent Savolainen³

One of the biggest challenges for conservation biology is to provide conservation planners with ways to prioritize effort. Much attention has been focused on biodiversity hotspots¹. However, the conservation of evolutionary process is now also acknowledged as a priority in the face of global change². Phylogenetic diversity (PD) is a biodiversity index that measures the length of evolutionary pathways that connect a given set of taxa^{3,4}. PD therefore identifies sets of taxa that maximize the accumulation of 'feature diversity'. Recent studies, however, concluded that taxon richness is a good surrogate for PD^{5–9}. Here we show taxon richness to be decoupled from PD, using a biome-wide phylogenetic analysis of the flora of an undisputed biodiversity hotspot—the Cape of South Africa. We demonstrate that this decoupling has real-world importance for conservation planning. Finally, using a database of medicinal and economic plant use¹⁰, we demonstrate that PD protection is the best strategy for preserving feature diversity in the Cape. We should be able to use PD to identify those key regions that maximize future options, both for the continuing evolution of life on Earth and for the benefit of society.

The Cape of South Africa is an area of less than 90,000 km². Botanically, it is one of the most species-rich areas of the world. There are more than 9,000 plant species, of which about 70% are endemic¹¹. For decades it has been noted that a longitudinal gradient in species richness exists across the Cape¹². The western part, with a predominantly winter rainfall regime, has about twice the density of plant species of the eastern region, which receives rainfall year-round¹³. Higher species richness in the western part has been attributed to variation in speciation and extinction rates as a consequence of differences in historical ecological conditions¹⁴. In the west, species richness also varies with topography, with the more uniform lowlands having fewer species than the rugged mountain landscapes¹³. Similarly, there are higher numbers of endemic genera in the western part of the Cape¹⁵.

We collected and compiled distribution data for the entire Cape and created an inventory of species and genera per quarter-degree square (QDS; the finest scale available). After extensive fieldwork (2003–2005), we reconstructed the phylogeny of the Cape flora, on the basis of plastid ribulose-1,5-bisphosphate carboxylase/oxygenase large subunit (*rbcL*). We used an exemplar from 735 genera, each indigenous to the Cape. Because of computing limitations imposed by the size of the data matrix, phylogenetic relationships were

reconstructed using the parsimony ratchet¹⁶. Molecular branch lengths were optimized using maximum likelihood. Using non-parametric rate smoothing¹⁷, the branch lengths were then transformed to units of absolute time for PD calculation. This is the largest phylogenetic tree yet built for an entire flora.

We compared per-QDS species and genus richness with per-QDS PD (calculated as the length of the subtree that joins the genera in each QDS to the root of the tree³). As expected^{5–9}, we found these diversity indices to be distributed in a similar manner (Fig. 1b, c; linear regressions: PD versus species richness $R^2 = 0.77$, PD versus genus richness $R^2 = 0.96$). These results initially indicated a limited role for PD in conservation planning in this region^{6,8,18}. However, this similarity in overall distribution hides key differences in the distribution of these metrics. We found PD to scale with taxon richness, but the scaling to be complex: some regions have more or less PD than would be expected from their taxon richness. Using two tests (a loess regression of per-QDS PD on genus richness, Fig. 1d; and comparing the observed PD in each QDS against an empirical randomization of PD, Fig. 1e) we found a distinctive east–west division in the distribution of PD that broadly corresponds to the climatic zones defined previously¹³, with PD for a given number of taxa being higher in the eastern region than in the western.

These results demonstrate that the flora (within QDS) of the western part of the Cape is phylogenetically clustered: it is made up of relatively closely related genera, resulting from multiple radiations over at least the last 25 million years^{19–21}. This results in a higher proportion of both shared and short branches, relative to the east, and therefore a lower PD score for a given number of lineages. In contrast, the flora (within QDS) of the eastern region is phylogenetically 'over-dispersed' relative to the western region: it contains genera that are, on average, less closely related to one another. These patterns result from fundamental evolutionary and palaeoclimatic processes in the west^{22–24}. Relative over-dispersion in the east is likewise explicable: the eastern flora abuts another biodiversity hotspot (Maputaland–Pondoland–Albany), is highly ecotonal, and contains occasional exemplar genera from unusual ecotypes¹¹.

We found that these conflicting patterns of taxon diversity and PD invalidate the sole use of taxon richness for conservation actions. Conservation planning is not just about total numbers, but also about marginal gains. To mimic the critical decisions that conservation planners face in the Cape, we set up a series of conservation

¹South African National Biodiversity Institute, Kirstenbosch Research Centre, Private Bag X7, Claremont 7735, South Africa. ²Department of Botany, University of Cape Town, University Private Bag, Rondebosch 7700, South Africa. ³Jodrell Laboratory, Royal Botanic Gardens, Kew, Richmond, Surrey, TW9 3DS, UK. ⁴South African National Biodiversity Institute, Biodiversity Planning Unit, Private Bag X101, Pretoria 0001, South Africa. ⁵Biology Department, Gilmer Hall, University of Virginia, Charlottesville, Virginia 22904-4328, USA. ⁶Institute of Ecology, University of Georgia, Athens, Georgia 30602, USA. ⁷Botany Department, Nelson Mandela Metropolitan University, PO Box 77000, Port Elizabeth 6031, South Africa. ⁸Australian Museum, 6 College Street, Sydney, New South Wales 2010, Australia. ⁹Department of Zoology, University of Cambridge, Downing Street, Cambridge, CB2 3EJ, UK. ¹⁰Centre for Invasion Biology, Private Bag X1, University of Stellenbosch, Matieland 7602, South Africa. ¹¹Department of Botany and Plant Biotechnology, University of Johannesburg, PO Box 524, Auckland Park 2006, South Africa.

*These authors contributed equally to this work.

scenarios based upon complementarity. In each scenario, an additional locality that maximizes gain in a biodiversity index is to be included in an existing partial set of conservation areas. We initially chose additions to partial sets based upon taxon richness, and examined the marginal gain in PD experienced. We then contrasted these gains by choosing additions to partial sets based directly on PD. The results show that gains in taxon richness and gains in PD are decoupled (Fig. 2 and Supplementary Information). Typically, selection for conventional taxon complementarity misses localities that would provide large gains in PD.

Why does it matter that PD is not well captured by conventional taxon-based policies? We argue that maximizing PD is the best bet-hedging strategy. By maximizing feature diversity we maximize

option value: the possibility of having the right feature at hand in an uncertain future. We use a practical example to illustrate this point. We identified all genera in the Cape with species of medicinal or economic importance¹⁰. We divided these genera into three types of use (food, medicine and other). Using a randomization test, we found that each type of use is phylogenetically clumped (all $P < 0.01$) and that different categories of use are clustered in different parts of the phylogeny (Supplementary Information). So how should we have designed a conservation strategy to preserve useful plants if this distribution were not known? Simply choosing samples of the largest possible number of genera permits the selection of a set of genera that are themselves phylogenetically clumped: such a set might include many genera of one type of use but this must come at a cost to the

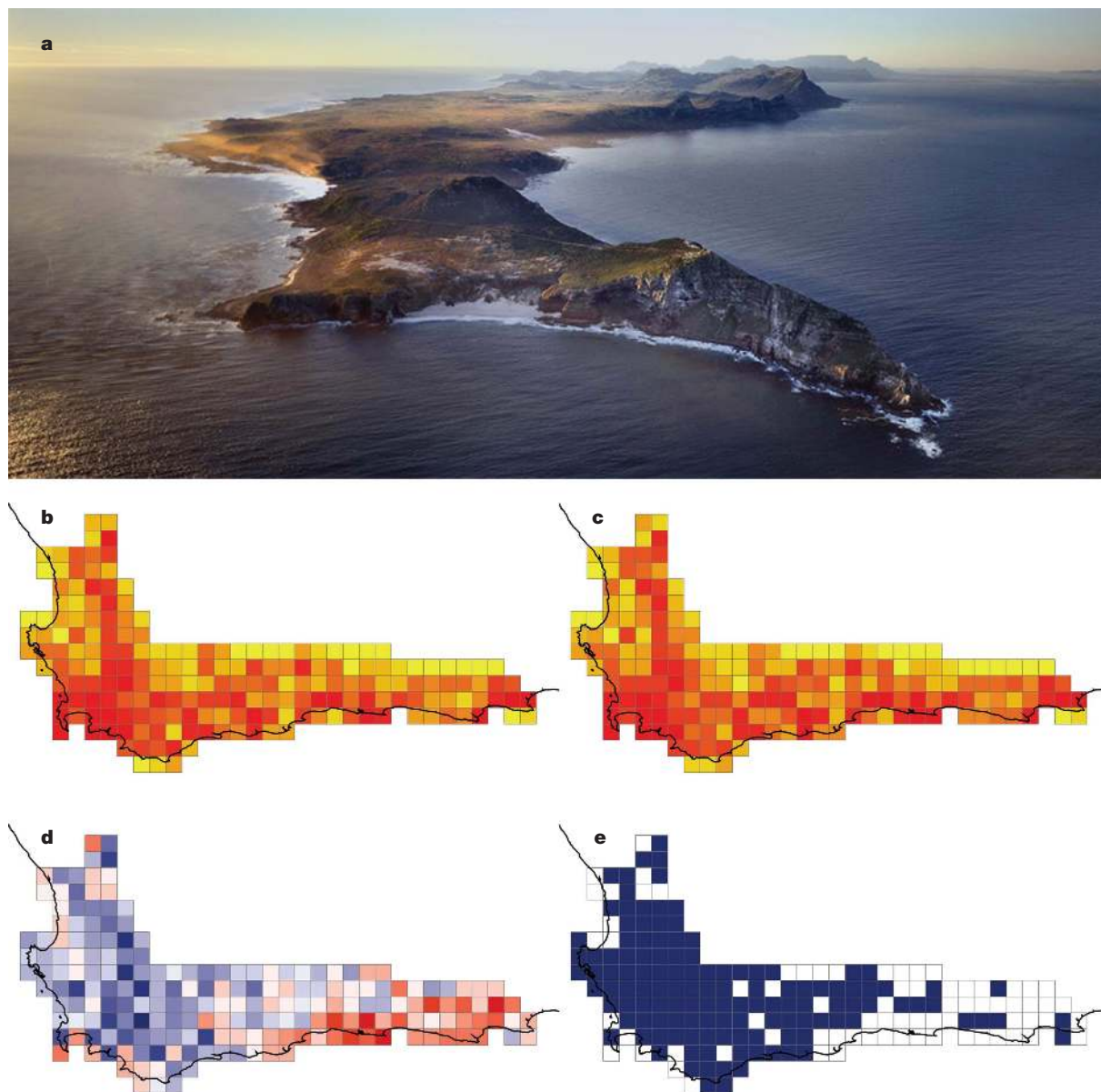


Figure 1 | Taxon richness and phylogenetic diversity in the Cape. **a**, This biodiversity hotspot, which includes the renowned Cape Peninsula, Cape of Good Hope and Table Mountain (in the distance), dominated by fynbos vegetation, is situated at the southern tip of Africa. Picture credit: A. Proust/iAfrika. **b–e**, Maps of 201 QDS covering the entire Cape region. **b**, Genus richness (ten quantile intervals from yellow to deep red). **c**, PD calculated using NPRS absolute age estimates in million years (colour code as for **b**). **d**, Residuals from a loess regression of PD (calculated using NPRS absolute age estimates) on genus richness. QDS with negative residuals are

indicated in blue, and those with positive residuals are shown in red (shading increments of half a standard deviation). **e**, The spatial distribution of unusual PD values, as assessed by comparing the observed PD in each QDS with 10,000 PD values calculated by random selection of the same number of genera from the Cape flora. Cells with significantly lower PD ($P < 0.05$, two-tailed) than expected are shaded in blue. A similar pattern was found when the tree was simplified to reflect the phylogeny-based taxonomy of the Angiosperm Phylogeny Group³⁰ (Supplementary Information).

other two types, because they are found in different parts of the phylogeny. Choosing a selection of over-dispersed taxa based on PD would have maximized the probability of having representatives of each of the three classes of use. In fact, we found that a set of cells chosen to maximize PD complementarity (blue line, Fig. 2) samples all useful genera in 13 QDS, while a set chosen to maximize taxon complementarity (black line, Fig. 2) requires 15 QDS to do so, although the majority of useful genera in both cases are sampled in the first few QDS. In an uncertain future, where we are not yet sure of the sort of plant features we will need, we argue that incorporating gains in PD into conservation planning is the best strategy.

It is not just our own options, though, that we need to keep open. We do not know the characteristics that species in the Cape will need to adapt and diversify in a future of climatic change. We therefore argue that maximizing PD will in turn maximize the options for future diversification. The many radiations in the western part of the Cape may well be a reason²⁵ to see the region as one of high evolutionary potential. However, although it is possible, we see no reason why future speciation regimes must be the same as those that gave rise to the historical diversification in the western part of the Cape. Throughout the history of angiosperms, diversification has been a complex process in which the propensity to diversify was highly labile and dependent upon many different traits at different times²⁶. Our recommendation would not be to reject recently diversifying sites in the west as conservation targets, but to ensure that PD is maximized by inclusion of suitable areas in the east into existing conservation schemes. Balancing these two diversity indices is now at least an algorithmic problem for which we have suitable tools²⁷. We also note that scale is important. For example, our phylogenetic tree does not include lineages that are not found in the Cape, but we have chosen the most biologically sound limits: a phylogeographic delimitation²⁸ that falls within a single country and can therefore be managed under a single coordinated conservation response²⁹. Any conservation plan that operates at less than a global scale will always be at risk of finding solutions that are optimal only within the region being considered.

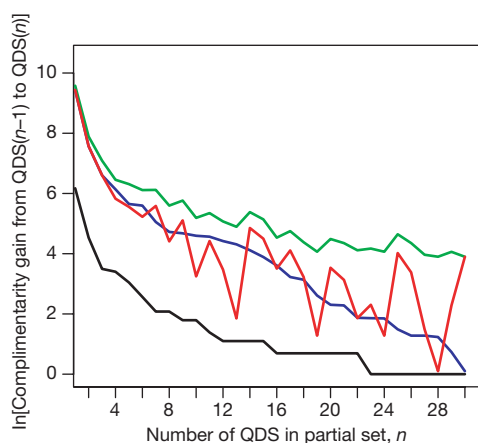


Figure 2 | Complementarity analysis of PD and genus richness. A series of conservation scenarios based on complementarity were set up with a simple greedy algorithm: for each partial set defined along the x axis, we identified the additional QDS that provided the highest possible genus-based complementarity (black). We then calculated the PD complementarity that would be provided by this same QDS (red), as well as the alternative additional QDS that would provide the highest possible PD complementarity (green). Whereas comparisons of diversity measures have usually focused on richness, it is now apparent that decision-making depends on marginal gains (complementarity values) and these must be the basis for comparisons. Here we show that gains in genus richness are poor predictors of gains in PD (contrast red and green lines). We also show the independent series of QDS that provide the highest PD-based complementarity (blue).

We have shown that a simple correspondence between taxon richness and PD can hide a fundamental decoupling of biodiversity indices, with drastically different conservation outcomes if only one of the indices is used. The Cape is one of the most well-studied hotspots, so our findings clearly raise the possibility that similar decoupling may be found in others. Further, we know from simulations⁷ that a decoupling of PD and taxon richness is most likely when the underlying phylogeny is unbalanced and there is strong phylogeographic structure; both these are epiphenomena of endemic radiations. We conclude by suggesting that because biodiversity hotspots are defined in part by their richness in endemics¹, they are precisely the areas in which a decoupling of PD and taxon richness is most likely—as is observed here.

METHODS

DNA sequencing and phylogeny reconstruction. We sampled one exemplar species for 735 of the 943 genera of angiosperms currently recognized in the Cape (~78%) and obtained sequence data for the plastid *rbcL* exon (ribulose-1,5-bisphosphate carboxylase/oxygenase large subunit). Phylogenetic relationships were reconstructed using the parsimony ratchet¹⁶ method with 15% of the characters perturbed and 200 iterations; ten independent parsimony ratchet searches were performed and the shortest trees resulting from these independent searches were used to create a consensus tree. Clade support was assessed with 500 bootstrap replicates. One of the most parsimonious trees from the parsimony ratchet analysis was chosen as a best hypothesis of relationships for the Cape plant genera. PD calculations were performed using branch lengths (maximum parsimony and maximum likelihood) and age estimates (non-parametric rate smoothing¹⁷; relative time divergences were transformed into absolute ages using twelve well-characterized fossils; see Supplementary Information).

Distribution of phylogenetic diversity. The distribution of genera within the Cape was compiled as a binary matrix of absence/presence per quarter degree square (QDS; approximately 25 km × 27 km) using data from the Pretoria National Herbarium database (PRECIS). The spatial pattern of the relationship between PD and taxon richness was revealed by plotting the residuals for a loess regression of per-QDS PD on taxon richness. To locate QDS with significantly higher or lower PD than expected from their taxon richness, the PD in each QDS was compared with 10,000 PD values for sets of genera of the same size, sampled without replacement (Supplementary Information).

Medicinal and economic species. A randomization procedure was used to assess whether the distribution of medicinal and economic species is constrained by the phylogeny or randomly distributed across lineages. To be considered of medicinal and/or economic use, a given genus must have at least one species found in the Cape that is recorded in the database of the Survey of Economic Plants for Arid and Semi-Arid Lands (SEPASAL¹⁰; Supplementary Information).

Received 27 October 2006; accepted 9 January 2007.

- Myers, N., Mittermeier, R. A., Mittermeier, C. G., da Fonseca, G. A. B. & Kent, J. Biodiversity hotspots for conservation priorities. *Nature* **403**, 853–858 (2000).
- Mace, G. M., Gittleman, J. L. & Purvis, A. Preserving the tree of life. *Science* **300**, 1707–1709 (2003).
- Faith, D. P. Conservation evaluation and phylogenetic diversity. *Biol. Conserv.* **61**, 1–10 (1992).
- Vane-Wright, R. I., Humphries, C. J. & Williams, P. H. What to protect? Systematics and the agony of choice. *Biol. Conserv.* **55**, 235–254 (1991).
- Brooks, T. M. et al. Global biodiversity conservation priorities. *Science* **313**, 58–61 (2006).
- Polasky, S., Csuti, B., Vossler, C. A. & Meyers, S. M. A comparison of taxonomic distinctness versus richness as criteria for setting conservation priorities for North American birds. *Biol. Conserv.* **97**, 99–105 (2001).
- Rodrigues, A. S. L., Brooks, T. M. & Gaston, K. J. in *Phylogeny and Conservation* (eds Purvis, A., Gittleman, J. L. & Brooks, T. M.) 101–119 (Cambridge University Press, Cambridge, UK, 2005).
- Rodrigues, A. S. L. & Gaston, K. J. Maximising phylogenetic diversity in the selection of networks of conservation areas. *Biol. Conserv.* **105**, 103–111 (2002).
- Torres, N. M. & Diniz, J. A. F. Phylogenetic autocorrelation and evolutionary diversity of Carnivora (Mammalia) in conservation units of the New World. *Genet. Mol. Biol.* **27**, 511–516 (2004).
- Survey of Economic Plants for Arid and Semi-Arid Lands. (SEPASAL) database (<http://www.rbghkew.org.uk/ceb/sepasal/internet/>) (Royal Botanic Gardens, Kew, London, 1999).
- Goldblatt, P. & Manning, J. C. Plant diversity of the Cape region of southern Africa. *Ann. Missouri Bot. Gard.* **89**, 281–302 (2002).
- Linder, H. P. The radiation of the Cape flora, southern Africa. *Biol. Rev.* **78**, 597–638 (2003).

13. Cowling, R. M. & Lombard, A. T. Heterogeneity, speciation/extinction history and climate: explaining regional plant diversity patterns in the Cape floristic region. *Divers. Distrib.* **8**, 163–179 (2002).
14. Cowling, R. M., Cartwright, C. R., Parkinson, J. E. & Allsopp, J. C. Fossil wood charcoal assemblages from Elands Bay Cave, South Africa: implications for Late Quaternary vegetation and climates in the winter-rainfall fynbos biome. *J. Biogeogr.* **26**, 367–378 (1999).
15. Linder, H. P. & Midgley, J. J. Taxonomy, compositional biodiversity and functional biodiversity of fynbos. *S. Afr. J. Sci.* **90**, 329–333 (1994).
16. Nixon, K. C. The parsimony ratchet, a new method for rapid parsimony analysis. *Cladistics* **15**, 407–414 (1999).
17. Sanderson, M. J. A nonparametric approach to estimating divergence times in the absence of rate constancy. *Mol. Biol. Evol.* **14**, 1218–1231 (1997).
18. Williams, P. H. & Humphries, C. J. in *Biodiversity: a Biology of Numbers and Difference* (ed. Gaston, K. J.) (Blackwell Science, Oxford, UK, 1996).
19. Goldblatt, P. *et al.* Radiation in the Cape flora and the phylogeny of peacock irises *Moraea* (Iridaceae) based on four plastid DNA regions. *Mol. Phyl. Evol.* **25**, 341–360 (2002).
20. Linder, H. P. Evolution of diversity: the Cape flora. *Trends Plant Sci.* **10**, 536–541 (2005).
21. Richardson, J. E. *et al.* Rapid and recent origin of species richness in the Cape flora of South Africa. *Nature* **412**, 181–183 (2001).
22. Cowling, R. M. & Proches, S. in *Plant Diversity and Complexity Patterns: Local, Regional and Global Dimensions* (eds Friis, I. & Balslev, H.) 273–288 (The Royal Danish Academy of Sciences and Letters, Copenhagen, 2005).
23. Midgley, G. F., Hannah, L., Roberts, R., MacDonald, D. J. & Allsopp, J. Have Pleistocene climatic cycles influenced species richness pattern in the greater Cape Mediterranean Region? *J. Mediterr. Ecol.* **2**, 137–144 (2001).
24. Proches, S., Wilson, J. R. U. & Cowling, R. M. How much evolutionary history in a 10x10 m plot? *Proc. R. Soc. Lond. B* **273**, 1143–1148 (2006).
25. Erwin, T. L. An evolutionary basis for conservation strategies. *Science* **253**, 750–752 (1991).
26. Davies, T. J. *et al.* Darwin's abominable mystery: insight from a supertree of the angiosperms. *Proc. Natl Acad. Sci. USA* **101**, 1904–1909 (2004).
27. Wilson, K. A., McBride, M. F., Bode, M. & Possingham, H. P. Prioritizing global conservation efforts. *Nature* **440**, 337–340 (2006).
28. Goldblatt, P. & Manning, J. C. *Cape Plants, a Conspectus of the Cape Flora in South Africa* (National Botanical Institute of South Africa, Cape Town, South Africa, 2000).
29. Mooers, A. O., Heard, S. B. & Chrostowski, E. in *Phylogeny and Conservation* (eds Purvis, A., Brooks, T. L. & Gittleman, J. L.) (Oxford Univ. Press, Oxford, 2005).
30. APG. An update of the Angiosperm Phylogeny Group classification for the orders and families of flowering plants: APG II. *Bot. J. Linn. Soc.* **141**, 399–436 (2003).

Supplementary Information is linked to the online version of the paper at www.nature.com/nature.

Acknowledgements We thank E. Arnold, K. Balele, W. Barrington, N. Bergh, F. Conrad, L. Csiba, C. Cupido, A. Dold, the Fourcade Botanical Club, K. Davis, J. Donaldson, P. Drew, T. Fulcher, G. Gardiner, J. Gittleman, P. Goldblatt, N. Helme, E. Kapinos, A. Khunou, N. B. Lester, A. Mabunda, M. Powell, D. Snijman, K. Tolley, T. Trinder-Smith, A. G. Verboom, E. van Jaarsveld, S. Vetter, C. Williams, M. Wolfson, F. Woodvine, and especially I. Nänni, for assistance; the conservation authorities of the Western, Eastern and Northern Cape in South Africa for granting collecting permits as well as the managers of nature reserves and private landowners; A. Proust/iAfrika for the picture in Fig. 1; and T. Barraclough, M. Chase and H. Possingham for comments on the manuscript. We thank the Darwin Initiative for the Survival of Species, the South African National Biodiversity Institute, the University of Cape Town, the Royal Botanic Gardens Kew, the Bentham-Moxon Trust, the US National Science Foundation, the University of Virginia and the European Commission (HOTSPOTS/EDIT) for funding.

Author Information DNA sequences have been deposited at GenBank/EMBL under accession numbers AM234779–AM235167 (see also Supplementary Information). Reprints and permissions information is available at www.nature.com/reprints. The authors declare no competing financial interests. Correspondence and requests for materials should be addressed to F.F. (f.forest@kew.org) and V.S. (v.savolainen@kew.org).

the Fe nucleus, thus decreasing δ . In contrast, the removal of an electron from the redox-active ligand orbital has a minor effect on δ (e.g., $\delta = -0.15$ mm/s for $[\text{Fe}^{\text{IV}}(\text{B}^*)(\text{O})]^-$ compared with $\delta = -0.12$ mm/s for $[\text{Fe}^{\text{IV}}(\text{B}^*)(\text{O})]^{2-}$) (table S5). Inspection of the DFT results shows that the Fe-O bond of **3** has nearly the same covalency as the Fe-O bonds in $\text{Fe}^{\text{IV}}=\text{O}$ complexes (12, 17, 18). The calculated unpaired spin density on the oxo group of **3** is 0.22, which is less than expected (≈ 0.4) by comparison with $\text{Fe}^{\text{IV}}=\text{O}$ complexes (≈ 0.8); the difference can be traced to a spin polarization of the bonding ($p_x + d_{xz}$) orbital. The exchange potential generated by the d_{yz}^{α} electron places the virtual d_{xz}^{α} level below the d_{xz}^{β} level. As a consequence, the transfer of electron density from p_x^{α} to d_{xz}^{α} is greater than from p_x^{β} to d_{xz}^{β} , resulting in a negative spin density in p_x , which, combined with the positive spin density for p_y (~ 0.4), yields a net spin density of less than 0.4.

The z axis of Eq. 1 parallels the Fe-O bond within 5° . The unpaired electron in the d_{yz} orbital produces a large negative x component of the spin-dipolar part of the A tensor, $A_{(s-d)/g_N\beta_N} = (-24.4, +8.7, +15.7)$ T, and together with the isotropic contact term gives the larger A value along x . Owing to the large energy gaps between the narrowly spaced (d_{xz}, d_{yz}) pair and the other 3d levels, spin-orbit coupling acts primarily between d_{xz} and d_{yz} and produces (i) an effective g value $g_z = 2(1 - \zeta/\Delta)$ (g_x and g_y are not affected) and (ii) an orbital contribution to the mag-

netic hyperfine interaction, $A_{Lz}I_zS_z$, where $A_{Lz} = P(g_z - 2) \approx -13$ T. Substitution of $\zeta = 260 \text{ cm}^{-1}$ and $\Delta_{\text{DFT}} = 2000 \text{ cm}^{-1}$ gives the observed value $g_z = 1.74$ and $A_{Lz} = -13$ T (19).

Complex **3** thus appears to have a low-spin d^3 configuration in contrast to a recently described isoelectronic manganese(IV)-oxo complex (20), which is high spin, $S = 3/2$, by EPR criteria. Our particular interest in TAML-catalyzed reactions pertains to their proven potential in green chemistry. The present work provides an opportunity to elucidate elementary steps in the catalytic cycles of TAML activators by taking advantage of the high purity of **3**, with its various prominent spectroscopic signatures, as a stoichiometric reagent.

References and Notes

1. I. G. Denisov, T. M. Makris, S. G. Sligar, I. Schlichting, *Chem. Rev.* **105**, 2253 (2005).
2. E. I. Solomon *et al.*, *Chem. Rev.* **100**, 235 (2000).
3. M. Costas, M. P. Mehn, M. P. Jensen, L. Que Jr., *Chem. Rev.* **104**, 939 (2004).
4. D. N. Harischandra, R. Zhang, M. Newcomb, *J. Am. Chem. Soc.* **127**, 13776 (2005).
5. M. Newcomb *et al.*, *J. Am. Chem. Soc.* **128**, 4580 (2006).
6. N. Aliaga-Alcalde *et al.*, *Angew. Chem. Int. Ed.* **44**, 2908 (2005).
7. A. Chanda *et al.*, *J. Inorg. Biochem.* **100**, 606 (2006).
8. A. Ghosh *et al.*, *J. Am. Chem. Soc.* **127**, 2505 (2005).
9. D. Banerjee *et al.*, *Angew. Chem. Int. Ed.* **45**, 3974 (2006).
10. S. S. Gupta *et al.*, *Science* **296**, 326 (2002).
11. M. J. Bartos *et al.*, *Coord. Chem. Rev.* **174**, 361 (1998).
12. M. R. Bukowski *et al.*, *Science* **310**, 1000 (2005).
13. J.-U. Rohde *et al.*, *Science* **299**, 1037 (2003).
14. Materials and methods are available as supporting material on Science Online.

15. The 3d spin-flip transition ($d_{xy}^{\beta} \rightarrow d_{xz}^{\alpha}$) is higher in energy than the ligand-to-metal transition ($\pi_p^{\beta} \rightarrow d_{xz}^{\alpha}$), where π_p is the redox-active orbital of the phenyl moiety, owing to the large $\{d_{xz}, d_{yz}\} - d_{xy}$ splitting.
16. J. T. Groves, *J. Inorg. Biochem.* **100**, 434 (2006).
17. A. Decker, M. D. Clay, E. I. Solomon, *J. Inorg. Biochem.* **100**, 697 (2006).
18. F. Neese, *J. Inorg. Biochem.* **100**, 716 (2006).
19. The free-ion value for the one-electron spin-orbit coupling constant ζ is 580 cm^{-1} (21). Given the high degree of covalency of **3**, the adopted ζ is not unreasonable. $P = 2 g_N \beta \beta_N \langle r^{-3} \rangle_{3d}$ has been taken as 50 T.
20. T. H. Parsell, R. K. Behan, M. P. Hendrich, A. S. Borovik, *J. Am. Chem. Soc.* **128**, 8728 (2006).
21. J. Bendix, M. Brorson, C. E. Schaffer, *Inorg. Chem.* **32**, 2838 (1993).
22. The work was supported by NIH grants EB001475 (E.M.) and GM-38767 (L.Q.), the Heinz Endowments (T.J.C.), Environmental Protection Agency (grant RD 83 to T.J.C.), and the Heinz Foundation for the Teresa Heinz Scholars for Environmental Research award (to D.B.). XAS data were collected on beamline X3B at the National Synchrotron Light Source, which is supported by the U.S. Department of Energy and the National Institutes of Health. We also thank M. Costas and A. Ghosh for valuable suggestions.

Supporting Online Material

www.sciencemag.org/cgi/content/full/1133417/DC1
Materials and Methods
SOM Text
Figs. S1 to S3
Tables S1 to S6
References

3 August 2006; accepted 12 December 2006
Published online 21 December 2006;
10.1126/science.1133417
Include this information when citing this paper.

Small Phytoplankton and Carbon Export from the Surface Ocean

Tammi L. Richardson^{1*} and George A. Jackson²

Autotrophic picoplankton dominate primary production over large oceanic regions but are believed to contribute relatively little to carbon export from surface layers. Using analyses of data from the equatorial Pacific Ocean and Arabian Sea, we show that the relative direct and indirect contribution of picoplankton to export is proportional to their total net primary production, despite their small size. We suggest that all primary producers, not just the large cells, can contribute to export from the surface layer of the ocean at rates proportional to their production rates.

Carbon export from the oceanic surface layer is controlled by biological transformations that occur within the pelagic food web (1, 2). Autotrophic picoplankton ($< 2 \mu\text{m}$ in diameter) often dominate primary production in these regions but are believed to contribute relatively little to carbon export from surface layers because of their small sizes, slow sinking rates, and rapid utilization in the microbial loop.

Large, rapidly sinking phytoplankton, such as diatoms, are believed to control carbon flux from upper ocean layers, and their contributions to export are believed to be disproportionately larger than their contributions to total primary production (1). Here we ask whether the contributions of picoplankton to carbon fluxes from the surface ocean are, in fact, disproportionately low.

Using results from inverse and network analyses of U.S. Joint Global Ocean Flux Study (JGOFS) data from the equatorial Pacific (EqPac) and Arabian Sea, we show that the relative contributions of various phytoplankton size classes to carbon export are proportional to their contributions to total net primary production (NPP) (3) (Fig. 1). Potential export pathways

include direct routes, such as aggregation and incorporation into settling detritus, and indirect export through the consumption of picoplankton aggregates by organisms at higher trophic levels. The network analysis used in these studies (4) estimates the total particulate organic carbon (POC) flux that originated from each input source, here the NPP of each phytoplankton size class. In the EqPac, for example, picoplankton contributed 70% or more of the total NPP measured during JGOFS EqPac time series cruises and were responsible for 87% of POC export via detritus and 76% of carbon exported through the mesozooplankton (5). Mesozooplankton consumed both picoplankton-derived detritus and picoplankton-fed micrograzers. Similarly, at a northern station in the Arabian Sea during the Northeast Monsoon, picoplankton NPP was 86% of the total and was the source for 97 and 75% of the total carbon exported from the euphotic zone via the POC and mesozooplankton pathways, respectively (6). The relative contributions of the picoplankton to carbon export decreased where they produced relatively less of the total NPP but were nonetheless substantial (Fig. 1 and Table 1).

We believe that the contributions of picoplankton to carbon flux from oceanic surface layers have been overlooked because of assumptions that are made about cell size, sinking dynamics, and the trophic pathways of picoplankton through ecosystems. The seminal paper

¹Marine Sciences Program and Department of Biological Sciences, University of South Carolina, Columbia, SC 29208, USA. ²Department of Oceanography, Texas A&M University, MS 3146, College Station, TX 77843-3146, USA.

*To whom correspondence should be addressed. E-mail: richardson@biol.sc.edu

by Smayda (7) documented the tendency of larger cells to sink faster. However, there are at least three potential mechanisms for increasing the effective size of picoplankton and their removal rates from the euphotic zone. First, the aggregation of picoplankton cells into larger detrital particles (8, 9) enhances their vertical settling velocities and resulting export fluxes (10–12). A simple model of aggregation and cell sinking for phytoplankton of varying diameters (3) (Fig. 2) shows that, at peak velocities, the average settling rate for aggregated cells from 1 to 30 μm in diameter is similar, although aggregation does not substantially increase the settling rates of the largest cells modeled (100 μm). We conclude that an individual alga does not need to be large to sediment out, even though settling rates are generally faster for single cells that are larger. Aggregation may be enhanced if cells are nutrient-depleted (13), and settling may be enhanced by the incorporation of mineral matter (14–16).

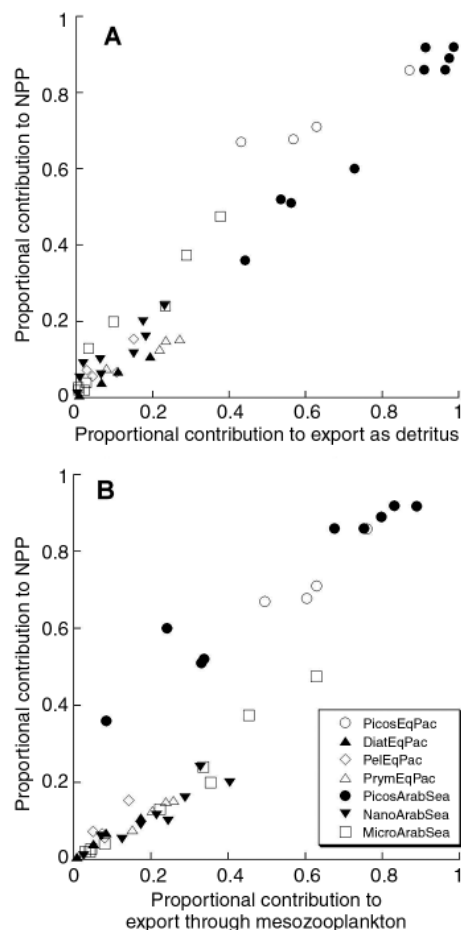


Fig. 1. Proportional contributions of varying phytoplankton groups or size classes (picoplankton, diatoms, pelagophytes, and prymnesiophytes for the EqPac study and pico-, nano-, and microphytoplankton for the Arabian Sea) to NPP versus their proportional contributions to export as detritus (A) or through consumption of mesozooplankton (B). Proportional contributions were calculated as NPP or export due to the size class/total NPP or export flux.

The inclusion of small phytoplankton in marine snow aggregates is well documented (2, 17–19). Aggregates of intact *Emiliania huxleyi* were first found in sediment traps deployed for short time periods (24 to 48 hours) in the North Sea (20). In the northeast Atlantic, water samples captured with bottles showed concentrations of *Synechococcus*-like cyanobacteria on aggregates that were 3000 to 12,000 times higher in concentration than that seen in free-living forms (18). Picoplankton aggregates have also been observed in sediment traps equipped with acrylamide gels during short-term (48 hours) deployments in high-nutrient, low-chlorophyll waters off New Zealand (19). It is noteworthy that observations of aggregates of small phytoplankton in sediment traps have been in traps deployed for short time periods, which will minimize loss of material and maximize potential identification of constituent organisms as compared to longer-term deployments (21).

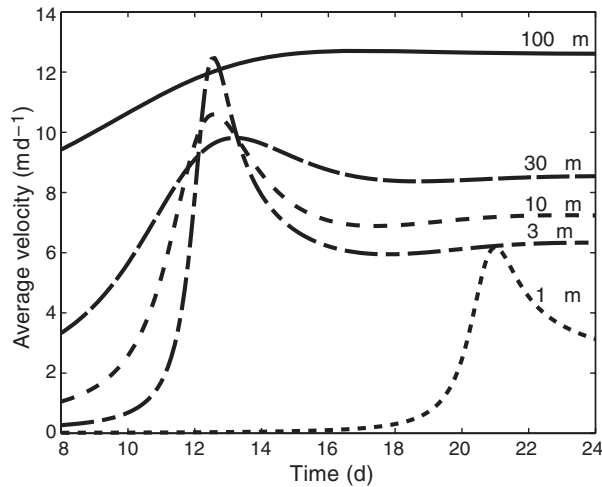
Although we did not explicitly include the process of aggregation in our EqPac and Arabian Sea analyses, we did allow ungrazed picoplankton production to flow directly to the detritus pool, where it could settle out as detritus or be consumed

by larger zooplankton. Models of food webs and biogeochemical cycling (22–25) generally assume that all picoplankton production is cycled through the microbial loop and that none sinks from the euphotic zone directly. This follows the classic analysis of pelagic community structure and nitrogen fluxes by Michaels and Silver (1), who assumed that “only large particles, with consequently high potential sinking rates, can exit the euphotic zone” and that “large colonies of smaller algae” decompose (and are presumably recycled) within the euphotic zone. Implicit in these food web structures is the assumption that growth and grazing in picoplankton-dominated open oceans are in balance over long (annual) time scales (26). However, our studies (5, 6) and those of others (27) have shown that microzooplankton grazing does not always balance picoplankton growth on shorter time scales (weeks to months). Food web models that force all picoplankton production through the microbial loop and do not allow direct picoplankton export may, therefore, be misleading. The conclusion of Michaels and Silver (1) that “picoplankton, the dominant producers in the model, contribute little to the sinking material” was based on a model (theirs) that was

Table 1. Direct and indirect contributions of picoplankton to carbon export from the euphotic zone for two cruises in the EqPac and at three stations (N7, S2, and S11) during three seasons in the Arabian Sea. Abbreviations are as follows: TS1, time series 1 (March to April 1992); TS2 Early, time series 2 cruise (early October 1992); TS2 Mid, midway through TS2 (mid-October 1992); TS2 Late, late October 1992; NEM, Northeast Monsoon; SIM, Spring Intermonsoon; and SWM, Southwest Monsoon.

Model	Export pathway	Carbon export due to picoplankton (mmol of C m ⁻² day ⁻¹)	% Contribution of picoplankton to total carbon export flux
<i>EqPac</i>			
TS1	POC	1.7	87
	Mesozooplankton	10.4	76
TS2 Early	POC	0.7	57
	Mesozooplankton	11.5	60
TS2 Mid	POC	1.5	43
	Mesozooplankton	11.0	50
TS2 Late	POC	1.7	63
	Mesozooplankton	11.2	63
<i>Arabian Sea</i>			
NEM N7	POC	1.0	97
	Mesozooplankton	11.5	75
NEM S2	POC	3.8	56
	Mesozooplankton	5.0	33
NEM S11	POC	4.3	99
	Mesozooplankton	11.1	83
SIM N7	POC	3.7	73
	Mesozooplankton	3.4	24
SIM S2	POC	5.9	92
	Mesozooplankton	2.4	89
SIM S11	POC	2.8	98
	Mesozooplankton	11.0	80
SWM N7	POC	2.3	91
	Mesozooplankton	1.7	68
SWM S2	POC	13.8	53
	Mesozooplankton	1.4	34
SWM S11	POC	10.5	44
	Mesozooplankton	0.8	1

Fig. 2. Average sinking velocity versus time (in days) for phytoplankton cells with diameters of 1, 3, 10, 30, and 100 μm . A cell density was assigned that is consistent with the velocity versus cell diameter graph of Smayda (7) for 3-, 10-, 30-, and 100- μm cells. Because 1- μm cells are outside the range analyzed by Smayda, a density difference of 0.0725 g cm^{-3} , characteristic of *Synechococcus lividus*, was used (3). Cells grow exponentially in a mixed layer of constant thickness, and there was no light or nutrient limitation. Algal cells collide to form aggregates at rates that depend on their abundances as well as sizes.



Large cells settle faster than small ones. With time, cell concentrations increase, causing an increase in the fraction of material in aggregates. The resulting increase in average particle size leads to an increase in average settling speed. Peaks in total cell concentration occur when the enhanced losses due to settling balance the gains due to cell division. The maximum average settling rate for particles formed from the 1- μm cells is not substantially different from that for particles formed from the 30- μm cells.

structured in such a way that no other conclusion could be reached.

A second pathway for the accelerated sinking of picoplankton-derived material is through mesozooplankton grazing. Picoplankton are usually considered to be too small to be captured effectively by larger grazers such as copepods (28), but the increase in effective size through aggregation makes them available and thus can enhance their export from surface layers through their incorporation into fast-sinking fecal pellets (9). When mesozooplankton consume picoplankton-containing aggregates, the picoplankton carbon short-circuits the microbial loop and results in higher than expected efficiency of carbon transfer from the euphotic zone (18, 29, 30). For animals such as salps that are capable of feeding on particles as small as 1 μm , aggregation is unnecessary to produce fecal pellets. The aggregates described in (19) were thought to originate in salp or other tunicate fecal material. The incorporation of picoplankton-sized particles into the rapidly sinking mucous nets and feces of filter feeders such as salps or pteropods provides an additional route for picoplankton removal (2, 31).

We propose, therefore, that the conventional view of carbon cycling, in which picoplankton carbon is recycled within the microbial loop and only larger phytoplankton carbon is exported, should be revised to include the alternative pathways for picoplankton carbon cycling discussed above. This alternative view relies on aggregation as a mechanism for both direct sinking (the export of picoplankton as POC) and mesozooplankton- or large filter feeder-mediated sinking of picoplankton-based production, but we believe that the evidence for both these processes under an array of environmental conditions is well established. Despite their small size, picoplankton may contribute more to oceanic carbon export than is currently recognized, and these contributions should be considered in current models of trophic dynamics in the ocean.

References and Notes

1. A. F. Michaels, M. W. Silver, *Deep-Sea Res.* **35**, 473 (1988).
2. L. Legendre, J. Le Fèvre, *Aquat. Microb. Ecol.* **9**, 69 (1995).
3. Materials and methods are available as supporting material on Science Online.
4. R. E. Ulanowicz, *NETWRK4: A Package of Computer Algorithms to Analyze Ecological Flow Networks* (Chesapeake Biological Laboratory, Univ. of Maryland, Solomons, MD, 1987).
5. T. L. Richardson, G. A. Jackson, H. W. Ducklow, M. R. Roman, *Deep-Sea Res. I* **51**, 1245 (2004).
6. T. L. Richardson, G. A. Jackson, H. W. Ducklow, M. R. Roman, *Deep-Sea Res. II* **53**, 555 (2006).
7. T. J. Smayda, *Oceanogr. Mar. Biol. Ann. Rev.* **8**, 353 (1970).
8. P. Albertano, D. DiSomma, E. Capucci, *J. Plankton Res.* **19**, 1405 (1997).
9. K. Olli, A.-S. Heiskanen, *J. Mar. Syst.* **23**, 165 (1999).
10. G. A. Jackson, *Deep-Sea Res.* **37**, 1197 (1990).
11. G. A. Jackson, *Deep-Sea Res. I* **48**, 95 (2001).
12. G. A. Jackson, A. M. Waite, P. W. Boyd, *Geophys. Res. Lett.* **32**, L13067 (2005).
13. M. E. Klut, J. G. Stockner, *Can. J. Fish. Aquat. Sci.* **48**, 1092 (1991).
14. H. D. R. Gomes, J. I. Goes, A. H. Parulekar, *J. Plankton Res.* **14**, 1307 (1992).
15. C. Klass, D. E. Archer, *Global Biogeochem. Cycles* **16**, 1116 (2002).
16. R. A. Armstrong, C. Lee, J. I. Hedges, S. Honjo, S. G. Wakeham, *Deep-Sea Res. II* **49**, 219 (2002).
17. N. Revelante, M. Gilmartin, *J. Exp. Mar. Biol. Ecol.* **146**, 217 (1991).
18. R. S. Lampitt, K. E. Wishner, C. M. Turley, M. V. Angel, *Mar. Biol.* **116**, 689 (1993).
19. A. M. Waite, K. A. Safi, J. A. Hall, S. D. Nodder, *Limnol. Oceanogr.* **45**, 87 (2000).
20. G. C. Cadée, *Mar. Ecol. Prog. Ser.* **24**, 193 (1985).
21. K. O. Buesseler et al., *Report of SCOR Working Group 116* (International Council of Scientific Unions, Woods Hole, MA, 2006).
22. R. B. Rivkin et al., *Science* **272**, 1163 (1996).
23. P. W. Boyd, P. P. Newton, *Deep-Sea Res. I* **46**, 63 (1999).
24. E. A. Laws, *Global Biogeochem. Cycles* **14**, 1231 (2000).
25. F. Chai, R. C. Dugdale, T.-H. Peng, F. P. Wilkerson, R. T. Barber, *Deep-Sea Res. II* **49**, 2713 (2002).
26. M. R. Landry et al., *Limnol. Oceanogr.* **42**, 405 (1997).
27. M. R. Roman et al., *Deep-Sea Res. II* **49**, 175 (2002).
28. P. Nival, S. Nival, *Limnol. Oceanogr.* **21**, 24 (1976).
29. U. Passow, A. L. Alldredge, *J. Plankton Res.* **21**, 2203 (1999).
30. X. Mari, F. Rassoulzadegan, *Mar. Ecol. Prog. Ser.* **279**, 13 (2004).
31. T. T. Noji et al., *J. Plankton Res.* **19**, 863 (1997).
32. This work was supported by NSF (grants OCE 0097296 and OCE 0352127 to G.A.J.).

Supporting Online Material

www.sciencemag.org/cgi/content/full/315/5813/838/DC1
Materials and Methods
References

4 August 2006; accepted 20 December 2006
10.1126/science.1133471

Integration of TGF- β and Ras/MAPK Signaling Through p53 Phosphorylation

Michelangelo Cordenonsi, Marco Montagner, Maddalena Adorno, Luca Zacchigna, Graziano Martello, Anant Mamidi, Sandra Soligo, Sirio Dupont, Stefano Piccolo*

During development and tissue homeostasis, cells must integrate different signals. We investigated how cell behavior is controlled by the combined activity of transforming growth factor- β (TGF- β) and receptor tyrosine kinase (RTK) signaling, whose integration mechanism is unknown. We find that RTK/Ras/MAPK (mitogen-activated protein kinase) activity induces p53 N-terminal phosphorylation, enabling the interaction of p53 with the TGF- β -activated Smads. This mechanism confines mesoderm specification in *Xenopus* embryos and promotes TGF- β cytostasis in human cells. These data indicate a mechanism to allow extracellular cues to specify the TGF- β gene-expression program.

Cross-talk between signaling pathways is necessary to effect efficient and fine-tuned regulatory control over metazoan development and physiology. TGF- β and receptor tyrosine kinase (RTK) ligands are pleiotropic cytokines affecting several aspects of cell behavior,

ranging from differentiation and proliferation to movement and survival (1, 2). Previous work has shown that these signaling pathways are integrated: The Ras/MAPK cascade, which is downstream of RTK signaling, affects TGF- β -induced mesoderm development in vertebrate